Nanoscale

PAPER

View Article Online
View Journal

Cite this: DOI: 10.1039/d5nr04997k

Probing thermal stability in $CsPbI_3$ quantum dots with coupled Pb-site doping and halide passivation

Pouriya Naziri, [a,b] Saba Sepahban Shahgoli, [a,b] Hadi Jahangiri [c] and Umut Aydemir *[b,d]

All-inorganic $CsPbI_3$ quantum dots (QDs) exhibit exceptional optoelectronic properties but suffer from poor thermal and structural stability, hindering their device integration. Here, we systematically investigate the temperature-dependent stability of pristine and Pb-site-substituted QDs combined with halide surface passivation, namely $CsPb_{0.95}Co_{0.05}I_3$ and $CsPb_{0.95}Ag_{0.05}I_3$, within the 20–80 °C range. Comprehensive X-ray diffraction (XRD), transmission electron microscopy (TEM), photoluminescence (PL), time-resolved photoluminescence (TRPL), UV-visible absorption (UV-Vis), and Fourier-transform infrared (FTIR) measurements reveal that dual cation-halide doping ($CoCl_2$ + CoI_2 or AgCl + AgI) enhances lattice rigidity, mitigates thermal expansion, and suppresses nonradiative recombination. While pristine $CsPbI_3$ QDs show α-phase distortion and emission quenching above 60 °C, doped QDs retain a cubic morphology and bright PL up to 80 °C. Lifetime analysis confirms reduced thermally activated non-radiative rates ($\Delta k_{nr} \approx 6.7 \times 10^{-3}$ ns^{-1} for Co^{2+}-doped and 5.6×10^{-3} ns^{-1} for Ag^{+}-doped *versus* 1.48×10^{-2} ns^{-1} for pristine QDs), evidencing significant trap suppression. The smallest lattice dilation ($\Delta d \approx 0.6\%$) and minimal bandgap narrowing ($\Delta E_g \approx 0.055$ eV) observed in Ag-doped QDs demonstrate superior thermal robustness. These findings elucidate a synergistic stabilization mechanism in which B-site substitution strengthens lattice bonding and halide passivation reinforces surface anchoring, providing a practical route toward thermally durable $CsPbI_3$-based optoelectronic materials.

Received 26th November 2025,
Accepted 1st February 2026

DOI: 10.1039/d5nr04997k

rsc.li/nanoscale

1. Introduction

All-inorganic cesium lead halide perovskite QDs ($CsPbX_3$, X = Cl, Br, I) have emerged as a new class of semiconductor nanomaterials,[1] offering near-unity photoluminescence quantum yields, sharp emission features, and compositionally adjustable bandgaps suitable for energy conversion devices and light emitting diodes (LEDs).[2–4] Among these, iodide-based $CsPbI_3$ QDs stand out for red and near-infrared optoelectronic applications due to their narrower bandgap and favorable radiative recombination dynamics.[5,6] In bulk form, $CsPbI_3$ readily transforms from the photoactive black cubic α-phase to the non-perovskite δ-phase below approximately 300 °C under ambient conditions, driven by its low Goldschmidt tolerance factor.[7,8]

At the nanoscale, surface and quantum confinement effects kinetically stabilize the α-phase, mitigating its inherent metastability.[9,10] Swarnkar *et al.* reported that $CsPbI_3$ QDs preserve the cubic phase for extended periods under ambient conditions.[11] However, degradation eventually occurs through ligand desorption,[12] halide migration,[13] and defect formation[14] under environmental or thermal stress. Consequently, the thermal resilience of $CsPbI_3$ nanostructures is primarily dictated by lattice strain, vacancy concentration, and the effectiveness of surface passivation.[15] Therefore, their widespread implementation remains limited by inherent phase instability and thermal degradation under ambient or elevated temperature conditions, particularly during device operation.[14,16]

To overcome these challenges, dopant engineering[10,17,18] offers a powerful strategy to tune lattice energetics and reduce defect densities in $CsPbI_3$ QDs. Introducing smaller or aliovalent cations (Mn^{2+},[19] Co^{2+},[3] Zn^{2+},[20] Sr^{2+},[21] Ag^{+},[8] Yb^{3+} [22]) at the Pb-site has been widely explored as a strategy to improve phase stability. By carefully selecting dopant ions with suitable ionic radii and chemical properties, it is possible to reinforce the perovskite lattice, effectively reducing lattice strain and miti-

[a]Graduate School of Sciences and Engineering, Koç University, Istanbul-34450, Türkiye
[b]Koç University Boron and Advanced Materials Application and Research Center (KUBAM), Istanbul-34450, Türkiye. E-mail: uaydemir@ku.edu.tr
[c]Koç University Surface Science and Technology Center (KUYTAM), Istanbul-34450, Türkiye
[d]Department of Chemistry, Koç University, Istanbul-34450, Türkiye

gating the phase transition from the metastable α-phase to the undesirable δ-phase.[23] However, aliovalent Pb-site doping can also introduce charge-mismatch constraints and complex defect or surface chemistry, meaning that improved phase stability cannot be inferred from composition alone. Hence, complementary surface-passivation strategies are often required to further suppress defect formation and preserve emission under thermal stress. In this context, halide passivation plays a pivotal role in improving the structural and optical stability of perovskite QDs by mitigating surface-related defects.[24,25] The incorporation of halide-rich environments or ionic additives enables anions such as Cl^-, Br^-, and I^- to coordinate with undercoordinated Pb^{2+} sites, thereby reducing trap-state density and suppressing nonradiative recombination.[3,8] Such passivation also limits ion migration, promotes smoother surface morphology, and strengthens ligand-surface interactions, collectively contributing to enhanced overall stability.[26] Nevertheless, organic ligands (*e.g.*, oleic acid and oleylamine) are prone to detachment under thermal stress, which exposes reactive sites and accelerates degradation.[16] Alternatively, multi-anchor ligands and halide-enriched surface layers provide stronger interfacial bonding and greater thermal durability.[14,27] Thus, the combined approach of cationic doping and halide co-passivation offers an effective route toward robust, defect-tolerant, and thermally stable all-inorganic perovskite QDs with sustained optoelectronic performance.[28,29]

Crucially, the effectiveness of these lattice and surface-level strategies is ultimately determined under thermal stress. Temperature plays a crucial role in dictating the excitonic behavior, electronic band structure, and lattice symmetry of halide perovskite QDs. As temperature increases, enhanced phonon–exciton coupling and thermal lattice expansion lead to bandgap narrowing, PL red-shift, linewidth broadening, and intensity quenching.[30] The extent of these effects is strongly dependent on halide composition. Among $CsPbX_3$ QDs, iodide-rich systems typically exhibit the most pronounced thermal sensitivity due to the relatively weak Pb–I bond strength and the presence of soft lattice phonons.[31] Comparative analyses across $CsPbCl_3$, $CsPbBr_3$, and $CsPbI_3$ compositions confirmed that iodide-based perovskites possess the lowest thermal tolerance, often undergoing earlier phase transformation and defect activation under heating.[32]

In recent years, temperature-dependent optical studies have provided valuable insights into exciton–phonon interactions and structural stability. For instance, $CsPbBr_3$ nanocrystals displayed systematic PL quenching and well-defined exciton–phonon coupling constants across a broad temperature range,[33] and further optical studies revealed that bandgap narrowing and PL red-shifts at elevated temperatures arise from lattice expansion and enhanced exciton–phonon coupling, consistent with quantum confinement behavior observed in $CsPbX_3$ nanocrystals.[34] Similarly, temperature-cycling PL and absorption measurements on $CsPbI_3$ thin films[35] and single-nanocrystal studies[36] revealed partially reversible phase transitions up to ~375 K, followed by irreversible lattice distortion and defect formation beyond this threshold. These findings highlight how heating not only modifies optical properties but also accelerates ion migration, trap activation, and local lattice deformation, ultimately destabilizing the photoactive α-phase.[37]

Despite extensive efforts to enhance the phase and chemical stability of $CsPbI_3$ QDs through cation doping and surface passivation, prior temperature-dependent studies on halide perovskite nanocrystals have predominantly focused on describing spectral or lifetime trends with temperature, or on isolating specific photophysical processes such as exciton-dopant energy transfer in non-iodide systems.[38] In parallel, many stabilization reports emphasize ambient aging, storage stability,[39,40] or post-annealing[41] behavior rather than continuous operational thermal stress. As a result, the temperature-dependent evolution of nonradiative recombination pathways and their direct correlation with lattice distortion, surface degradation, and dopant chemistry in iodide-based $CsPbI_3$ QDs remain insufficiently understood. Here, we explicitly address this gap through a controlled temperature-dependent structural and optical investigation of pristine and doped $CsPbI_3$ QDs with mixed-halide surface passivation. By correlating XRD and TEM tracked lattice stability with steady-state PL and temperature-resolved TRPL dynamics, we directly link dopant-halide chemistry to thermally activated loss mechanisms, establishing a mechanistic framework for suppressing nonradiative recombination and delaying structural degradation under operational thermal stress.

In this study, we present a comprehensive temperature-dependent structural and optical investigation of $CsPbI_3$, $CsPb_{0.95}Co_{0.05}I_3$, and $CsPb_{0.95}Ag_{0.05}I_3$ QDs (Fig. 1). Building on our earlier works on Co^{2+}-doped[3] and Ag^+-doped[8] $CsPbI_3$ QDs, where we systematically compared single-halide and mixed-halide precursor pairs (CoI_2 + $CoCl_2$ and AgI + AgCl), we previously showed that mixed-halide doping ($CsPb_{1-x}Co_xI_3$ with x = 0.025 $CoCl_2$ + 0.025 CoI_2; $CsPb_{1-x}Ag_xI_3$ with x = 0.025 AgCl + 0.025 AgI) yields the most pronounced improvements in optical and structural stability. Motivated by these results, we now examine the thermal robustness of these optimized mixed-halide QDs and benchmark them against pristine $CsPbI_3$ over a temperature range of 20–80 °C. Integrated structural and optical analyses reveal clear correlations between dopant-halide chemistry, lattice stability, and exciton dynamics. In summary, the coupled Pb-site substitution and halide passivation strategy enables remarkable thermal stabilization of $CsPbI_3$ QDs by simultaneously reinforcing the lattice and preserving surface passivation. Structural analyses confirm that doped QDs retain the cubic α-phase up to 80 °C, while pristine $CsPbI_3$ undergoes lattice distortion and optical quenching near 60 °C. Complementary PL, TRPL, and FTIR measurements reveal that mixed doped QDs suppress thermally activated nonradiative recombination (Δk_{nr} reduced by over 60%), mitigate ligand desorption, and preserves excitonic emission at elevated temperatures. Together, these findings demonstrate that lattice-surface co-engineering effectively delays phase transition and trap activation, providing a prom-

ising route to thermally robust, all-inorganic perovskite QDs with enhanced structural and optical resilience.

2. Experimental section

2.1. Materials

The following chemicals were employed without further purification: lead(II) iodide (PbI_2, 99.999%, Sigma-Aldrich), cesium carbonate (Cs_2CO_3, 99%, Sigma-Aldrich), 1-octadecene (ODE, 90%, Sigma-Aldrich), oleylamine (OAm, 70%, Sigma-Aldrich), oleic acid (OA, 90%, Sigma-Aldrich), methyl acetate (MeOAc, ≥99.5%, Tekkim), and hexane (≥95%, Sigma-Aldrich). For doping studies, cobalt chloride ($CoCl_2$, anhydrous, 99.7%, Alfa Aesar), cobalt iodide (CoI_2, 99.999%, Thermo Scientific), silver chloride (AgCl, anhydrous, 99.7%, Alfa Aesar), and silver iodide (AgI, 99.999%, Thermo Scientific) were used as dopant precursors. Hexane was used as the dispersion solvent throughout the experiments.

2.2. Synthesis of cesium oleate precursor

Cesium oleate (Cs-oleate) was synthesized following standard procedures from our previous stuides.[3,8] In brief, 0.4 g of Cs_2CO_3, 40 mL of ODE, and 1.6 mL of OA were combined in a three-neck flask and degassed at 120 °C under vacuum for 30 minutes. After two nitrogen purging cycles, the clear Cs-oleate solution was kept at 100 °C under nitrogen for immediate use in QD synthesis.

2.3. Synthesis of pristine, cobalt-doped, and silver-doped $CsPbI_3$ quantum dots

Pristine and doped $CsPbI_3$ QDs were synthesized *via* a modified hot-injection method, following our previous protocols. The $CsPb_{0.95}Co_{0.05}I_3$, and $CsPb_{0.95}Ag_{0.05}I_3$ QDs feed ratios were selected based on our prior optimization studies, which established these mixed halide formulations as effective for stabilizing $CsPbI_3$ QDs.[3,8] In all cases, 0.8 g of PbI_2 was dissolved in 40 mL of ODE and degassed at 120 °C under vacuum for 1 hour, followed by nitrogen purging for 30 minutes.

For cobalt doping, CoI_2 was directly added to the PbI_2 precursor solution, while $CoCl_2$ was pre-dissolved in OAm at 70 °C for 90 minutes. For silver doping, AgCl and AgI were each pre-dissolved in OAm under the same conditions. The desired dopant solutions, along with 4 mL of OA and 4 mL of OAm, were added to the PbI_2 mixture, followed by an additional 30-minute degassing and a 10-minute nitrogen purge.

The mixture was then heated to 170 °C, followed by the rapid injection of 6.4 mL of preheated Cs-oleate solution. After 5 seconds, the reaction was quenched in an ice-water bath.

2.4. Purification of quantum dots

Pristine, cobalt-doped, and silver-doped $CsPbI_3$ QDs were purified using a standard precipitation–redispersion method. Crude QD solutions were first precipitated by adding methyl acetate (MeOAc, 1 : 3 volume ratio) and centrifuged at 8000 rpm for 5 minutes. The precipitate was redispersed in hexane and subjected to a second MeOAc precipitation, followed by centrifugation at 8000 rpm for 2 minutes. After redispersion in hexane, the solution was centrifuged again at 4000 rpm for 5 minutes to remove excess PbI_2 and Cs-oleate residues. The supernatant was stored at 4 °C in the dark for 48 hours, then gently decanted and centrifuged once more at 4000 rpm for 5 minutes. The resulting purified QDs were collected for optical characterization and temperature-dependent studies.

2.5. Characterization

The optical properties of the QDs were evaluated using a SHIMADZU UV-3600 UV-visible spectrophotometer to record absorption spectra, from which the bandgap energies were determined. PL spectra were collected using an Agilent Cary Eclipse Fluorescence Spectrophotometer. TRPL measurements were performed using an Edinburgh Instruments FLS1000 fluorescence spectrometer equipped with an integrating sphere. TRPL measurements were carried out using a time-correlated single-photon counting (TCSPC) module with a 377 nm pulsed laser (64 ps pulse width, 200 ns repetition period).

A Huber CC chiller was employed to control the temperature during UV and PL measurements. The dilution of QD samples for optical measurements was optimized based on concentrations yielding the highest PL quantum yield (PLQY) in our previous studies.[3,8]

FT-IR spectra were obtained using a Jasco FT/IR-6800 spectrometer equipped with a single-reflection diamond ATR accessory, operating in the 650–4000 cm^{-1} range. Each spectrum was collected with a 4 cm^{-1} resolution by averaging multiple scans to ensure a high signal-to-noise ratio. The measurements were performed to identify surface functional groups and ligand-binding characteristics in pristine and doped $CsPbI_3$ QDs, providing insights into their temperature-dependent chemical and structural stability.

XRD patterns were recorded on a Rigaku MiniFlex 600 diffractometer with Cu Kα radiation (λ = 1.5418 Å), over a 2θ range of 10–60° at a scanning speed of 1° per minute. For XRD analysis, QD samples were drop-cast from a 0.5 mg mL^{-1} hexane solution onto silicon wafers to form uniform thin films.

TEM images were acquired using a HITACHI HF5000 Cold-FEG S/TEM at 200 kV. Additional high-resolution TEM analysis was conducted on an FEI Tecnai F30-G2 microscope operating at 300 kV, featuring a Super-Twin lens, a field emission gun, a point resolution of 2.0 Å, and an information limit of ~1.2 Å. Images were captured using a 2k × 2k MultiScan CCD camera (Gatan Inc., USA).

For XRD, FTIR, and TEM analyses, each QD sample was heated to the designated target temperatures. Temperature-dependent measurements were carried out by gradually heating the QD solutions under controlled conditions. To reach each target temperature (*e.g.*, from 30 °C to 40 °C), the solutions were heated for approximately 10–12 minutes, followed by a 5-minute equilibration period to ensure thermal stabilization before data acquisition. This protocol was applied consistently for UV-Vis absorption and PL analyses. For TRPL and FTIR measurements, the samples were heated using a cali-

brated heater until the desired temperature was reached, maintaining comparable heating and stabilization times to ensure a uniform thermal history across all measurements. For XRD analysis, the colloidal QD solutions were pre-heated to the corresponding temperatures, and the silicon substrates were also pre-heated to minimize thermal mismatch and measurement errors during deposition and data collection. In TEM studies, the pristine samples were imaged prior to heating, and subsequently, thermally treated samples (~80 °C) were prepared and analyzed under identical imaging conditions. All measurements were conducted on the same day and within a narrow time window to minimize environmental variations and experimental inconsistencies.

3. Results and discussion

3.1. Temperature-dependent structural analysis of pristine and doped $CsPbI_3$ QDs

To investigate the structural evolution of pristine and doped $CsPbI_3$ QDs under thermal stress, XRD patterns were recorded for undoped $CsPbI_3$ and the optimally mixed-halide-doped samples $CsPb_{1-x}Co_xI_3$ (x = 0.025 $CoCl_2$ + 0.025 CoI_2) and $CsPb_{1-x}Ag_xI_3$ (x = 0.025 AgCl + 0.025 AgI) within the temperature range of 20–80 °C (Fig. 2).

All samples exhibit diffraction peaks characteristic of the cubic α-$CsPbI_3$ phase (ICSD 161481) with no detectable impurity reflections, confirming that Co^{2+} and Ag^+ ions are successfully incorporated into the perovskite lattice rather than forming separate metal halide phases. At room temperature, both doped samples exhibit a systematic shift of diffraction peaks toward higher 2θ values compared to pristine $CsPbI_3$ (Fig. 2a), indicating a slight lattice contraction. This contraction results from the substitution of larger Pb^{2+} ions (119 pm) with smaller Co^{2+} (72 pm) and Ag^+ (115 pm) cations, as confirmed in our previous reports.[3,8]

With heating up to 80 °C, no reflections corresponding to the non-perovskite δ-phase are observed, confirming that all QDs retain their perovskite structure upon heating (Fig. 2b–d). All compositions show a gradual shift of the (200) diffraction peak toward lower 2θ, indicative of positive thermal expansion (increasing interplanar spacing). Compared to the pristine sample, the doped QDs display smaller thermal expansion coefficients, behaving as chemically pressurized lattices with enhanced bond strength and greater resistance to thermally induced lattice distortion. We note, however, that the absolute magnitude of the peak shifts is not strictly quantitative because instrumental parameters (*e.g.*, sample height/displacement, packing, thermal-stage alignment) were not calibrated against an internal standard such as LaB_6. Accordingly, these peak-position changes are interpreted qualitatively.

In contrast, the pristine $CsPbI_3$ QDs exhibit a progressive decrease in the (100) peak intensity and noticeable broadening above 60 °C (Fig. 2b), signifying the buildup of microstrain and partial loss of long-range crystallinity. Meanwhile, $CsPb_{0.95}Co_{0.05}I_3$, and $CsPb_{0.95}Ag_{0.05}I_3$ QDs maintain sharp and intense reflections, demonstrating superior structural stability and suppressed thermally activated defect migration.

At around 80 °C, a weak shoulder appears adjacent to the main diffraction line in the pristine $CsPbI_3$ pattern (Fig. 2b). Rather than signifying decomposition, this secondary feature is attributed to the incipient formation of short-range orthorhombic (γ-like) domains or localized octahedral tilting within the cubic lattice, a transition frequently reported in $CsPbI_3$ QDs under moderate thermal or environmental stress. This observation is consistent with our earlier stability studies on

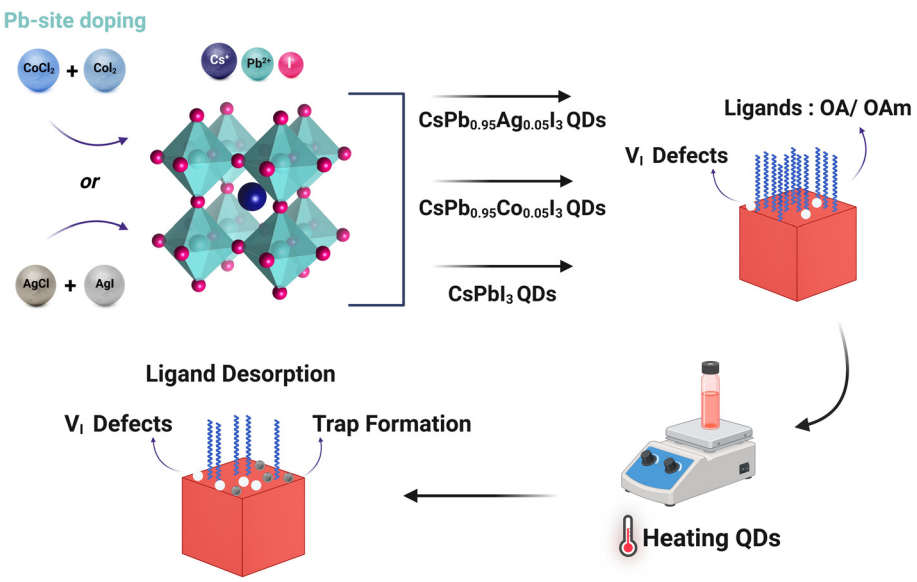

Fig. 1 Schematic representation of pristine $CsPbI_3$ QDs and doped counterparts $CsPb_{0.95}Co_{0.05}I_3$, and $CsPb_{0.95}Ag_{0.05}I_3$ QDs, showing the mixed-halide doping process ($CoCl_2$ + CoI_2 or AgCl + AgI) and the subsequent heating step used to investigate their thermal behavior.

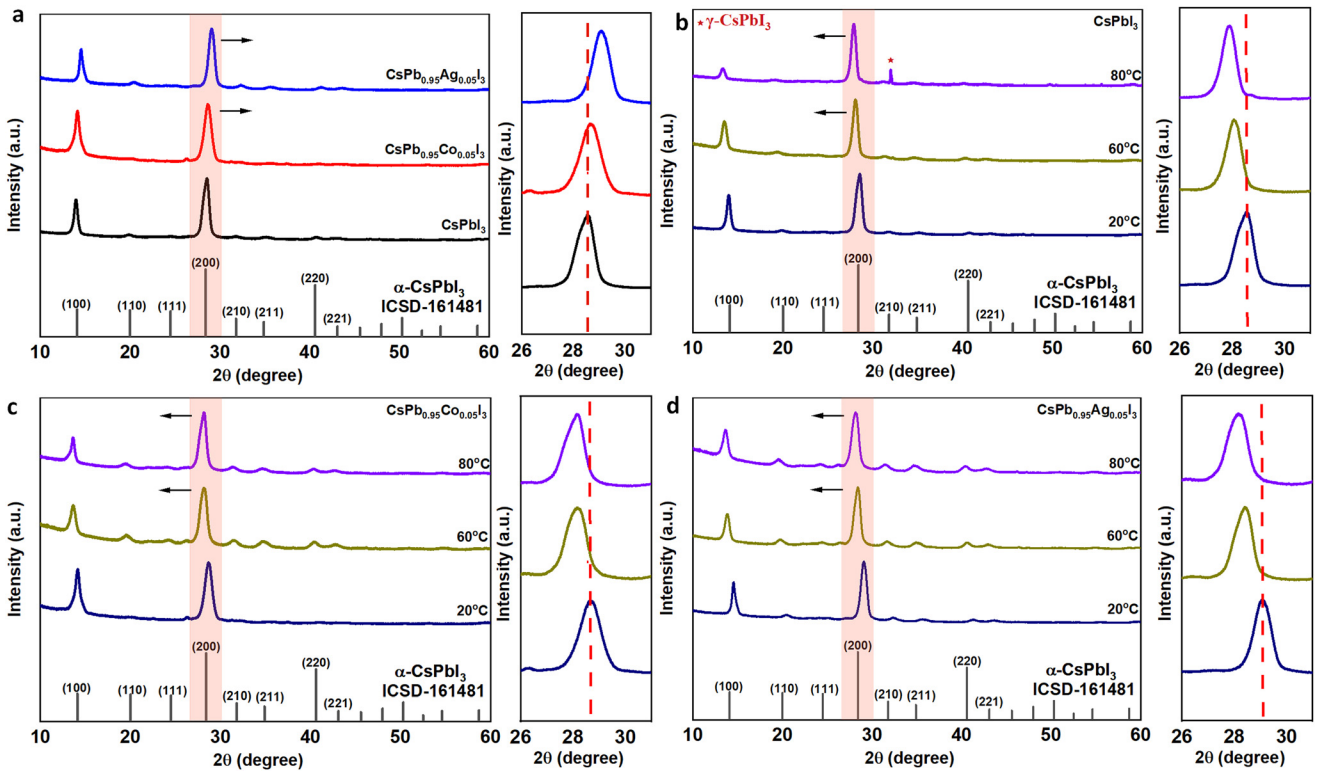

Fig. 2 Temperature-dependent XRD patterns of pristine and doped $CsPbI_3$ QDs: (a) comparison of pristine $CsPbI_3$, $CsPb_{0.95}Co_{0.05}I_3$, and $CsPb_{0.95}Ag_{0.05}I_3$ QDs at room temperature, showing peak shifts to higher 2θ values due to lattice contraction. (b–d) Temperature-dependent XRD patterns recorded between 20–80 °C for pristine $CsPbI_3$, $CsPb_{0.95}Co_{0.05}I_3$, and $CsPb_{0.95}Ag_{0.05}I_3$ QDs, respectively. With increasing temperature, all compositions exhibit a gradual shift toward lower 2θ, consistent with positive thermal expansion and increasing interplanar spacing.

cobalt and silver doped $CsPbI_3$ QDs,[3,8] where faint orthorhombic signatures emerged only after prolonged UV irradiation or aging, corresponding to slow lattice relaxation rather than irreversible α → δ transformation.

The absence of these orthorhombic distortions in $CsPb_{0.95}Co_{0.05}I_3$, and $CsPb_{0.95}Ag_{0.05}I_3$ QDs further confirms that dual cation-halide doping effectively suppresses thermally induced octahedral rotation, preserving the cubic α-phase throughout the temperature cycle. Collectively, these results demonstrate that Co^{2+} or Ag^{+} doping with Cl^{-}/I^{-} passivation not only enhances lattice rigidity but also delays structural relaxation pathways, thus extending the operational stability of $CsPbI_3$ QDs under elevated temperature conditions.

As context from our prior studies,[3,8] we previously employed XPS to probe the chemical environment and dopant distribution in pristine and doped $CsPbI_3$ QDs; no additional XPS measurements are included in this work, and detailed spectra/fitting results are available in those reports. In brief, the survey spectra confirmed the presence of Cs, Pb, and I as major elements, along with Co^{2+} and Ag^{+} in the doped samples, without detectable impurities, consistent with the XRD results. The Cs 3d peaks remained unchanged after doping, indicating that Cs^{+} ions at the A-site are unaffected by substitution. In contrast, the Pb 4f core-levels exhibited minor binding-energy shifts, reflecting local electronic modifications due to partial replacement of Pb^{2+} by Co^{2+} or Ag^{+}. Cl 2p peaks were observed in both doped samples but diminished after Ar^{+} ion etching, confirming that Cl^{-} resides mainly on the surface rather than in the lattice. This suggests that Cl^{-} ions act as surface passivators, compensating for iodine vacancies and reducing halide-related surface defects. These earlier observations support a combined doping-passivation picture in which B-site substitution and surface Cl^{-} passivation reduce iodine-vacancy-related traps, thereby suppressing nonradiative recombination and improving structural, optical, and thermal stability.

3.2. Thermal response and microstructural evolution of pristine and doped $CsPbI_3$ QDs

TEM was employed to investigate the morphological characteristics and thermal response of pristine, $CsPb_{0.95}Co_{0.05}I_3$, and $CsPb_{0.95}Ag_{0.05}I_3$ QDs. To evaluate the effect of temperature on their structural stability, TEM analyses including particle size distribution and lattice (*d*-spacing) measurements were performed before (BHT) and after heat treatment (AHT), as presented in Fig. 3.

All samples consist of well-defined cubic or slightly truncated nanocrystals with narrow size distributions, confirming the formation of the α-$CsPbI_3$ phase. The incorporation of Co^{2+} and Ag^{+} ions does not deteriorate the crystal morphology; instead, the doped QDs display enhanced shape uniformity

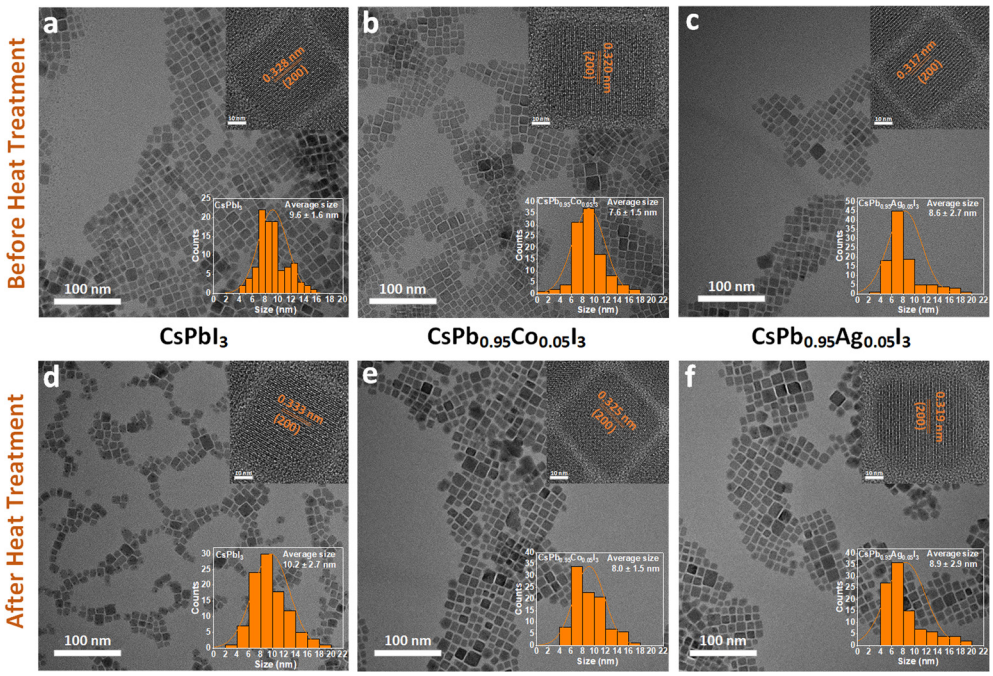

Fig. 3 TEM and HR-TEM images of (a and d) $CsPbI_3$, (b and e) $CsPb_{0.95}Co_{0.05}I_3$, and (c and f) $CsPb_{0.95}Ag_{0.05}I_3$ QDs before (top row) and after (bottom row) heat treatment. The inset histograms display particle-size distributions fitted with Gaussian functions, revealing narrow size dispersions and slight particle growth after heating. The HR-TEM insets show well-resolved lattice fringes corresponding to the (200) plane of the cubic α-phase with interplanar spacings of ~0.32–0.33 nm. All samples maintain high crystallinity and cubic morphology after thermal treatment, while Ag- and Co-doped QDs exhibit improved shape retention and reduced aggregation compared to pristine $CsPbI_3$, indicating enhanced structural stability upon heating.

and monodispersity. This improvement arises from the presence of smaller cations and mixed halide precursors ($CoCl_2$ + CoI_2 or AgCl + AgI), which finely regulate nucleation and growth kinetics by balancing surface energies and providing additional halide ligands that cap the QD surface during synthesis. At room temperature, the undoped $CsPbI_3$ QDs exhibit an average size of 9.6 ± 1.6 nm, whereas the Co^{2+} and Ag^+ doped QDs are slightly smaller, averaging 7.6 ± 1.5 nm and 8.6 ± 2.7 nm, respectively (Fig. 3a–c). The decrease in mean particle size is mainly attributed to the mixed-halide (Cl^-/I^-) synthesis environment, which alters nucleation-growth kinetics and strengthens surface passivation, leading to smaller and more uniform QDs. In parallel, the partial replacement of Pb^{2+} by smaller Co^{2+} and Ag^+ cations introduces a mild lattice contraction, as evidenced by the systematic shift of XRD peaks toward higher 2θ angles. This structural compression is further supported by HR-TEM observations: the $CsPb_{0.95}Ag_{0.05}I_3$ QDs display the smallest (200) lattice spacing (~0.317 nm), consistent with a more compact perovskite lattice. Overall, these findings indicate that halide passivation primarily governs particle size control, while cation substitution fine-tunes the lattice density, together yielding nanocrystals with improved uniformity and enhanced structural stability.

Upon heat treatment up to 80 °C (Fig. 3d–f), all samples largely preserve their cubic morphology and high crystallinity, evidencing robust structural resilience under mild thermal stress. However, subtle morphological differences emerge between the pristine and doped QDs. In pristine $CsPbI_3$, the nanocubes display edge rounding and corner truncation, indicative of mild surface reconstruction, likely driven by ligand desorption and ion migration, which reduces the sharpness of the {100} facets.

This is accompanied by a broader size/shape distribution and the appearance of locally fused or necked particles, indicating the early onset of thermally activated structural rearrangement as ligand density diminishes upon heating. Such surface restructuring is commonly attributed to oleic acid/oleylamine desorption and halide migration, which reduce surface passivation and promote facet reorganization.

By contrast, the $CsPb_{0.95}Co_{0.05}I_3$ QDs exhibit markedly improved morphological retention in which most nanocubes preserve well-defined edges and sharp corners, and the size distribution broadening is significantly suppressed. Only limited rearrangement is observed (Fig. 3e), suggesting that Co^{2+} incorporation and mixed Cl^-/I^- surface passivation effectively strengthen surface binding and mitigate heat-induced surface diffusion.

The $CsPb_{0.95}Ag_{0.05}I_3$ QDs exhibit the highest thermal robustness, retaining uniform cubic morphology and well-defined interparticle spacing even after heating. Minimal aggregation or rounding is observed, and the particle size histograms show nearly unchanged distributions (Fig. 3f). This exceptional stability arises from the synergistic effect of Ag^+ substitution and dual-halide passivation.

Moreover, the superior morphological stability of $CsPb_{0.95}Ag_{0.05}I_3$ QDs compared with $CsPb_{0.95}Co_{0.05}I_3$ QDs arises from differences in how the dopant cations stabilize both the lattice and the near-surface ionic framework under heating. Although both doped systems employ mixed halides (Cl^-/I^-), Ag^+ ($r \approx 115$ pm) is closer in size to Pb^{2+} ($r \approx 119$ pm), which favors gentler and more uniform lattice densification and reduces thermally induced lattice distortion, consistent with the smallest lattice dilation ($\Delta d \approx 0.6\%$). More importantly, Ag exhibits strong coordination with halide ions, stabilizing the near-surface halide environment and increasing the activation barrier for thermally activated halide redistribution and surface reconstruction processes that initiate coalescence in colloidal perovskite QDs. This reduced surface ion mobility directly suppresses diffusion-driven necking and particle fusion under thermal stress, thereby preserving QD morphology. Consistent with this mechanism, the Ag-doped sample also shows the smallest increase in nonradiative recombination (Δk_{nr}), indicating the strongest suppression of thermally activated loss channels.

Overall, these results show that while pristine $CsPbI_3$ QDs undergo slight morphological degradation upon heating, primarily due to ligand desorption and surface diffusion, the incorporation of Co^{2+} or Ag^+, together with Cl^-/I^- co-passivation, effectively suppresses these thermally activated processes. Substitution of Pb^{2+} by smaller Co^{2+} or Ag^+ ions strengthens local bonding and alleviates lattice strain. In parallel, the dual-halide environment enhances ligand anchoring and minimizes halide vacancy formation.

The lattice fringes in HR-TEM remain sharp and periodic in all cases, with (200) spacings clustering between 0.317–0.333 nm. A small, positive shift in d-spacing is observed upon heating 0.328 → 0.333 nm for pristine, 0.320 → 0.325 nm for $CsPb_{0.95}Co_{0.05}I_3$ QDs, and 0.317 → 0.319 nm for $CsPb_{0.95}Ag_{0.05}I_3$ QDs corresponding to an approximately 1.5% thermal expansion in pristine and Co^{2+}-doped samples, but only almost 0.6% in Ag^+-doped QDs. This subtle dilation matches the temperature-dependent XRD results, where diffraction peaks shifted to lower 2θ, confirming thermally induced lattice expansion. The smaller $\%\Delta d$ in the $CsPb_{0.95}Ag_{0.05}I_3$ QDs system indicates reduced thermal expansivity and greater lattice rigidity.

Statistical analysis of over 100 particles per composition reveals only minor increases in mean particle size upon heating (20–80 °C): from 9.6 ± 1.6 → 10.2 ± 2.7 nm for pristine $CsPbI_3$, 7.6 ± 1.5 → 8.0 ± 1.5 nm for $CsPb_{0.95}Co_{0.05}I_3$, and 8.6 ± 2.7 → 8.9 ± 2.9 nm for $CsPb_{0.95}Ag_{0.05}I_3$ QDs. The modest size increases (Δsize) reflect limited thermally induced coalescence. The pristine sample shows the largest broadening of its size distribution, indicating partial surface diffusion and ligand desorption, which can promote necking between adjacent nanocrystals. In contrast, Co-doped QDs display moderate stabilization, while Ag-doped QDs retain the sharpest facets, narrowest histograms, and most uniform spacing, indicating the highest thermal microstructural stability. These observations are summarized in Table 1.

The percentage changes in mean particle size (Δsize) and interplanar spacing (Δd) were quantitatively evaluated using the equations provided in the SI (section S1). Overall, both doped systems maintain their α-phase nanocube morphology and high crystallinity throughout the 20–80 °C range, in agreement with the XRD findings. These results confirm that mixed cation-halide doping not only refines QD size and uniformity during synthesis but also strengthens the lattice against thermal distortion and coalescence, thereby enhancing the structural robustness of $CsPbI_3$ QDs.

3.3. Thermal evolution of optical properties in pristine and doped $CsPbI_3$ QDs

3.3.1. Temperature-dependent PL emission behavior. To investigate the effect of heat treatment on the optical behavior of pristine and doped $CsPbI_3$ QDs, temperature-dependent steady-state PL measurements were carried out for $CsPbI_3$, $CsPb_{0.95}Co_{0.05}I_3$, and $CsPb_{0.95}Ag_{0.05}I_3$ samples, as shown in Fig. 4. Both doped systems exhibit a noticeable blue shift in their PL emission relative to pristine $CsPbI_3$ QDs, reflecting lattice contraction induced by cation substitution. This trend is consistent with the structural findings from XRD and TEM analyses, which confirmed lattice densification upon doping. Detailed structural-optical correlations for similar compositions have been reported in our previous studies.[3,8] Furthermore, the reduction in average PL lifetime (τ_{av}) observed for the doped QDs indicates that Co^{2+} and Ag^+ incorporation effectively modulates charge-carrier dynamics by suppressing iodine-vacancy (V_I) defects. Since these vacancies typically create shallow trap states that delay carrier recombination, their mitigation through combined cation substitution and halide passivation enhances radiative recombination efficiency and optical stability, thereby rendering the $CsPbI_3$ QDs more robust against temperature-induced degradation and improving overall thermal durability.

To establish a baseline for the subsequent temperature-dependent analysis, the photoluminescence spectra of pristine $CsPbI_3$, $CsPb_{0.95}Co_{0.05}I_3$ and $CsPb_{0.95}Ag_{0.05}I_3$ QDs were first

Table 1 Comparison of morphological and lattice parameters of $CsPbI_3$, $CsPb_{0.95}Co_{0.05}I_3$, and $CsPb_{0.95}Ag_{0.05}I_3$ QDs obtained from TEM and HR-TEM analyses before heat treatment (BHT) and after heat treatment (AHT)

Sample	Mean BHT ± SD (nm)	Mean AHT ± SD (nm)	Δsize (%)	(200) d_{BHT} (nm)	(200) d_{AHT} (nm)	Δd (%)
$CsPbI_3$	9.6 ± 1.6	10.2 ± 2.7	+6.3%	0.328	0.333	+1.5%
$CsPb_{0.95}Co_{0.05}I_3$	7.6 ± 1.5	8.0 ± 1.5	+5.3%	0.320	0.325	+1.5%
$CsPb_{0.95}Ag_{0.05}I_3$	8.6 ± 2.7	8.9 ± 2.9	+3.5%	0.317	0.319	+0.6%

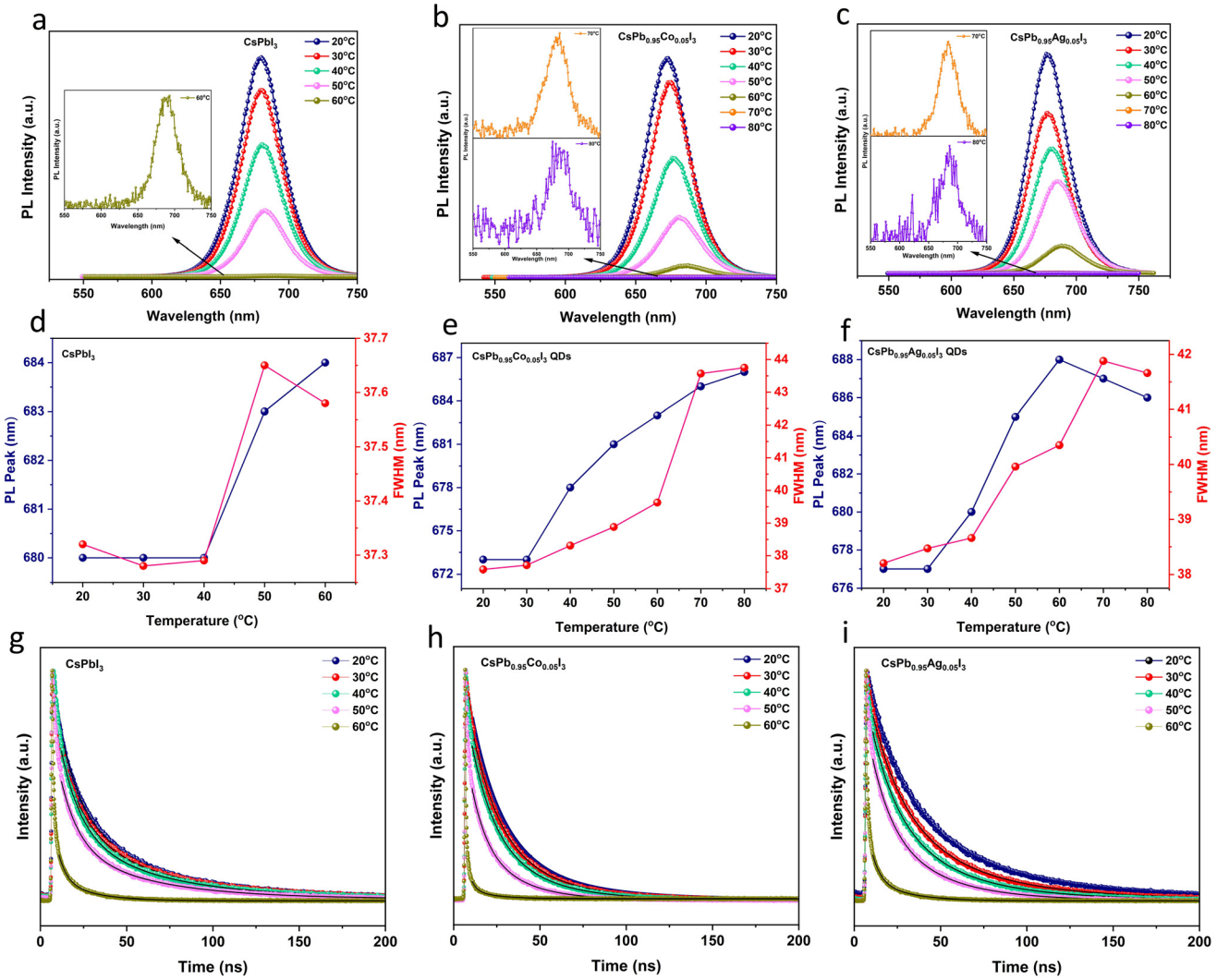

Fig. 4 Temperature-dependent steady-state and time PL characteristics of pristine $CsPbI_3$ (a, d and g), $CsPb_{0.95}Co_{0.05}I_3$ (b, e and h), and $CsPb_{0.95}Ag_{0.05}I_3$ (c, f and i) QDs. Panels (a–c) show normalized PL spectra recorded from 20 to 80 °C. The insets show representative spectra at elevated temperatures, where peak broadening becomes more pronounced and Gaussian fitting was applied to resolve the emission features. Panels (d–f) depict temperature-dependent variations of PL peak position and FWHM Panels (g–i) present time-resolved PL decay profiles measured at corresponding temperatures. Compared with pristine $CsPbI_3$, both Co- and Ag-doped QDs exhibit attenuated PL quenching, reduced peak broadening, and slower thermal redshift, confirming their superior optical and thermal stability under mild heating.

recorded at 20 °C under identical excitation conditions (Fig. S1). As shown, both doped samples exhibit a substantially enhanced PL intensity and improved spectral definition compared to pristine $CsPbI_3$, indicating a higher initial radiative recombination efficiency and reduced defect-assisted nonradiative pathways. This enhancement is consistent with effective Pb-site substitution combined with mixed-halide surface passivation, which lowers the density of trap states and improves exciton confinement. Importantly, the higher initial emission intensity and optical quality of the doped QDs provide a more favorable starting point under thermal stress, contributing to the delayed onset of luminescence quenching observed at elevated temperatures.

Temperature-dependent steady-state PL spectra (Fig. 4a–c) reveal a clear thermal quenching of the emission intensity for all samples as the temperature is raised. For pristine $CsPbI_3$, the PL intensity drops sharply at higher temperatures. This rapid loss of emission is consistent with thermally activated nonradiative recombination. As the lattice softens and surface ligands desorb, carriers are more efficiently captured by trap states instead of recombining radiatively. The onset of this asymmetric, weakened emission coincides with the structural instability of pristine $CsPbI_3$ observed by XRD and TEM, where early signs of lattice relaxation and particle coalescence appear near this same temperature window. Taken together, these results indicate that pristine $CsPbI_3$ QDs enter a regime of coupled optical and structural degradation at ~60 °C.

In contrast, both doped systems ($CsPb_{0.95}Co_{0.05}I_3$ and $CsPb_{0.95}Ag_{0.05}I_3$) maintain intense, spectrally well-defined PL beyond 60 °C and remain emissive up to 80 °C. The slower

quenching rate in the doped QDs indicates that the introduction of Co^{2+} or Ag^{+} together with mixed Cl^{-}/I^{-} halides suppress thermally activated nonradiative channels. This is consistent with two effects established in our structural analysis: (i) lattice stiffening and reduced thermal expansion, which delays octahedral distortion of the perovskite network, and (ii) enhanced surface passivation, which prevents ligand-loss-driven trap formation and slows coalescence. Among the doped samples, the Ag-containing QDs display the slowest PL quenching with temperature, retaining higher relative emission intensity at 70–80 °C. This behavior is attributed to stronger Ag-halide coordination at the surface, which is expected to heal iodine vacancies and strengthen ligand binding, thereby suppressing trap-assisted carrier loss even under thermal stress.

Although both doped systems remain emissive up to 80 °C, the PL spectra at 70 and 80 °C are less ideal than those at 20–60 °C, showing more pronounced broadening and slight line-shape distortion. This indicates that thermal quenching is not fully eliminated which is consistent with the intrinsic temperature sensitivity of $CsPbI_3$ QDs, but rather delayed and attenuated by the coupled effects of Pb-site substitution and mixed-halide surface chemistry. In this view, doping and passivation increases the activation barrier for thermally induced lattice softening and surface/ligand destabilization, so the dominant nonradiative pathways become significant only at higher temperature, shifting the onset of strong quenching from ~60 °C in pristine QDs toward ~70–80 °C in the doped samples.

The evolution of the PL peak position and the emission linewidth (FWHM), plotted in Fig. 4d–f, provides further insight into the thermal response. For all three compositions, increasing temperature generally drives a red-shift of the PL peak and a broadening of the FWHM. This trend is typical for perovskite QDs and reflects band-gap renormalization *via* lattice expansion and exciton–phonon coupling. As the crystal lattice expands and vibrational motion increases, the band gap narrows and the emission moves to longer wavelength, while exciton–phonon interactions and inhomogeneous carrier relaxation broaden the emission. This red-shift/broadening behavior is clearly visible and monotonically maintained over the lower-to-intermediate temperature range.

At elevated temperatures (≈ 60 °C for pristine $CsPbI_3$ and ≈ 70–80 °C for the doped samples), the apparent PL peak position and FWHM deviate from a simple monotonic trend. We attribute this to multi-channel recombination, meaning that the measured PL band becomes a superposition of at least two emissive channels whose relative weights change with temperature. Band-edge excitonic recombination from the electronically intact regions of the QDs, and thermally activated localized-state emission associated with shallow defect states or locally distorted near-surface regions (*e.g.*, halide-related surface environments) that possess slightly reduced effective band gaps. With increasing temperature, thermal activation promotes carrier exchange between these channels and shallow states can transiently trap carriers, and subsequent thermal release redistributes carriers between localized and band-edge states. This produces asymmetric line shapes (low-energy tails with weak shoulders) and a temperature-dependent change in the relative contribution of each channel. Consequently, when such spectra are fit using a single-peak model, the extracted peak position and FWHM represent a weighted average of overlapping components rather than a pure band-edge transition; as the localized-state fraction grows or saturates at the highest temperatures, the fitted peak can appear to level off or slightly reverse and the FWHM can show an apparent jump. Therefore, the observed non-monotonicity (≈ 1–3 nm) is a physical signature of temperature-activated mixed (band-edge + localized-state) emission, rather than random noise.

3.3.2. TRPL analysis. TRPL was employed to investigate the carrier recombination dynamics of pristine and doped $CsPbI_3$ QDs in the temperature range of 20–60 °C. The decay profiles were well fitted using a biexponential function (see section S2), yielding the τ_{av}. Biexponential fitting revealed two characteristic lifetimes, τ_1 attributed to fast nonradiative decay, and τ_2, related to slower radiative recombination dynamics.[42] A noticeable reduction in the average lifetime (τ_{av}) is observed after doping, suggesting that the introduction of dopant ions alters carrier recombination kinetics. The shorter τ_{av} reflects the suppression of iodine-vacancy-related shallow traps that would otherwise prolong carrier relaxation. All extracted fitting parameters are summarized in Tables S1–S3.

For pristine $CsPbI_3$ QDs, τ_{av} decreases significantly from 47.5 ns at 20 °C to 27.9 ns at 60 °C, accompanied by a progressive increase in the fast decay amplitude (A_1) and a reduction in τ_2. This pronounced shortening of τ_{av} reflects the thermally activated generation of shallow trap states and enhanced nonradiative recombination channels. At 60 °C, the PL peak asymmetry and broadening observed in Fig. 4a correlate with the emergence of such trap states, which likely arise from partial surface-ligand desorption and halide migration mechanisms known to diminish radiative efficiency and accelerate carrier recombination.

In $CsPb_{0.95}Co_{0.05}I_3$, τ_{av} remains consistently shorter (29.2 ns → 24.4 ns from 20 °C to 60 °C) than in pristine $CsPbI_3$, indicative of an intrinsically more efficient radiative decay pathway and reduced trap involvement. The smaller τ_2 and weaker temperature dependence signify that Co^{2+} incorporation and mixed-halide (Cl^{-}/I^{-}) coordination effectively passivate surface defects, limit iodine-vacancy formation, and stabilize the excitonic band edge. Although τ_{av} decreases slightly with temperature, this reduction arises primarily from radiative recombination acceleration rather than additional nonradiative losses, consistent with the enhanced morphological stability observed in TEM.

In $CsPb_{0.95}Ag_{0.05}I_3$ QDs, the recombination dynamics are the most thermally stable. The τ_{av} decreases only moderately from 39.3 ns at 20 °C to 32.2 ns at 60 °C. The slow component τ_2 remains long (≈ 35–44 ns) across the entire range, and the amplitude ratio (A_1/A_2) changes minimally, confirming that Ag^{+} doping *via* AgCl + AgI precursors produces stronger halide

passivation and enhanced surface-ligand anchoring. The dual-halide doping *via* AgCl and AgI precursors effectively passivates halide vacancies, thereby suppressing thermally activated carrier trapping. This defect mitigation results in stable radiative recombination dynamics and minimal PL quenching even at elevated temperatures.

3.3.3. Radiative and non-radiative recombination rates. To further evaluate how thermal stress activates nonradiative decay channels, the temperature evolution of τ_{av} was analyzed based on biexponential TRPL fits (Tables S1–S3).

The total recombination rate is described by:

$$\frac{1}{\tau_{av}(T)} = k_r(T) + k_{nr}(T) \quad (1)$$

where k_r and k_{nr} are the radiative and nonradiative recombination rates, respectively.

At 20 °C, the QDs are optimally passivated, thus, $\frac{1}{\tau_{av}(20)}$ is taken as the baseline recombination rate. The additional thermally activated nonradiative component at temperature T is estimated as:

$$\Delta k_{nr}(T) \approx \frac{1}{\tau_{av}(T)} - \frac{1}{\tau_{av}(20\,°C)} \quad (2)$$

Detailed lifetime-based derivations and calculations are provided in the SI (section S3) and the extracted Δk_{nr} values at 60 °C are summarized in Table 2. Quantitative comparison of the thermally activated nonradiative rate (Δk_{nr}) for all samples reveal that doping substantially suppresses the growth of nonradiative pathways with temperature.

At 60 °C, pristine $CsPbI_3$ QDs show a pronounced acceleration of recombination, τ_{av} drops from 47.5 ns to 27.9 ns, and the total recombination rate rises from ≈ 0.021 ns^{-1} to ≈ 0.0358 ns^{-1}, yielding $\Delta k_{nr} \approx 1.48 \times 10^{-2}$ ns^{-1}. This large increase indicates strong thermal activation of nonradiative pathways due to surface and halide-vacancy defects. The $CsPb_{0.95}Co_{0.05}I_3$ QDs exhibit a markedly smaller increase ($\Delta k_{nr} \approx 6.7 \times 10^{-3}$ ns^{-1}), consistent with partial trap suppression.

Dual doping with passivation limits iodine vacancy migration and maintains electronic coupling at the surface, slowing the activation of nonradiative centers. The $CsPb_{0.95}Ag_{0.05}I_3$ QDs show the slowest rise in recombination rate ($\Delta k_{nr} \approx 5.6 \times 10^{-3}$ ns^{-1}), confirming that Ag-halide dual doping most effectively inhibits trap activation. In this case, Ag^+ incorporation into the perovskite lattice stabilizes the inorganic framework, while the Cl^-/I^--rich surface environment passivates halide vacancies and improves ligand anchoring. As a result, radiative decay remains relatively stable and PL quenching is strongly suppressed, even under heating. These Δk_{nr} results provide direct quantitative evidence of how doping modulates thermal trap activation. Overall, cation substitution and halide passivation synergistically delay thermally induced nonradiative recombination, thereby extending the operational stability window of $CsPbI_3$-based QDs.

Taken together, these temperature-dependent PL and TRPL measurements establish three key insights. First, pristine $CsPbI_3$ QDs undergo rapid optical quenching and spectral distortion by ~60 °C, consistent with the emergence of incipient non-cubic domains in XRD and TEM, accompanied by minor surface relaxation and partial particle merging. Second, $CsPb_{0.95}Co_{0.05}I_3$ and $CsPb_{0.95}Ag_{0.05}I_3$ QDs maintain bright, well-defined emission up to 80 °C, demonstrating that mixed-cation substitution and halide passivation expand the thermal stability window of $CsPbI_3$ QDs by approximately 20 °C. Finally, although both doped systems eventually show mild PL asymmetry at the highest temperatures, their emission remains intense and their band-edge features intact, confirming that degradation is delayed rather than immediate.

Table 2 Calculated thermally activated nonradiative rate (Δk_{nr}) increments at 60 °C for pristine and doped $CsPbI_3$ QDs

Sample	Δk_{nr} (60 °C) (ns^{-1})
$CsPbI_3$	1.48×10^{-2}
$CsPb_{0.95}Co_{0.05}I_3$	6.7×10^{-3}
$CsPb_{0.95}Ag_{0.05}I_3$	5.6×10^{-3}

3.4. Temperature-dependent UV-Vis absorption behavior in pristine and doped $CsPbI_3$ QDs

The UV-Vis absorption spectra of pristine and doped $CsPbI_3$ QDs, recorded between 20 °C and 80 °C (Fig. 5), reveal characteristic temperature-induced band-edge evolution. All three samples exhibit a gradual redshift of the absorption onset with increasing temperature, accompanied by mild spectral broadening. This trend arises from thermally driven lattice expansion and enhanced electron–phonon coupling, which reduce the bandgap energy (E_g) according to the Varshni relation[43] (eqn (3)). The shift of the absorption edge is consistent with the redshift observed in the PL spectra, confirming that both absorption and emission processes are governed by the same temperature-dependent bandgap narrowing mechanism. For pristine $CsPbI_3$ (Fig. 5a), a noticeable broadening of the absorption edge occurs with increasing temperature, accompanied by a gradual loss of spectral definition around 60 °C. This behavior reflects enhanced structural disorder and reduced phase stability at elevated temperatures, consistent with the onset of non-cubic features observed in XRD and the decrease in PL symmetry and intensity. The weaker redshift in the doped samples indicates that cation substitution and halide complexation effectively reduce phonon-driven lattice fluctuations and stabilize the perovskite lattice under heat stress.

The extracted E_g values from Tauc plots are summarized in Table S4, showing a systematic decrease in bandgap energy with rising temperature for all samples. Specifically, pristine $CsPbI_3$ QDs narrow from 1.820 ± 0.003 eV at 20 °C to 1.772 ± 0.007 eV at 60 °C, while $CsPb_{0.95}Co_{0.05}I_3$ decreases from 1.832 ± 0.003 eV to 1.808 ± 0.006 eV over the same range. The $CsPb_{0.95}Ag_{0.05}I_3$QDs exhibit the smallest shift, from 1.820 ± 0.003 eV to 1.768 ± 0.007 eV, reflecting their superior thermal and structural stability.

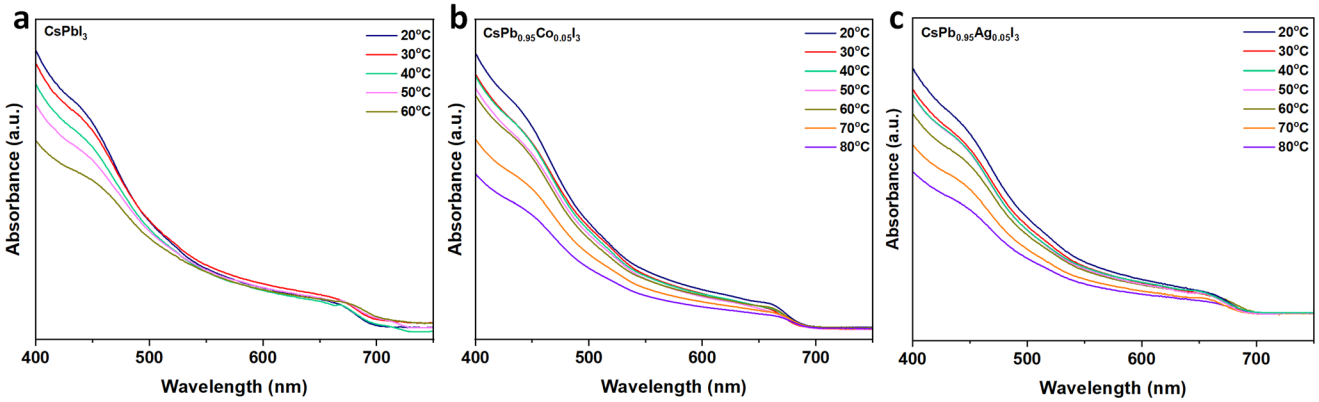

Fig. 5 Temperature-dependent UV-Vis absorption spectra of (a) pristine $CsPbI_3$, (b) $CsPb_{0.95}Co_{0.05}I_3$, and (c) $CsPb_{0.95}Ag_{0.05}I_3$ QDs measured between 20 °C and 80 °C.

This temperature dependence of E_g follows the Varshni relation:

$$E_g(T) = E_g(0) - \frac{\alpha T^2}{T + \beta} \quad (3)$$

where α and β are material-specific constants representing electron–phonon coupling and lattice expansion contributions, respectively. The redshift (bandgap narrowing) with temperature corresponds to enhanced electron–phonon interaction and thermal lattice dilation, which collectively reduce the energy separation between the valence and conduction bands.[44] Overall, the combined UV-Vis and Tauc plot analyses confirm that thermally induced bandgap narrowing dominates the optical response of $CsPbI_3$-based QDs. Doping with Co^{2+} and Ag^{+} ions significantly suppresses this effect, highlighting their role in reinforcing structural integrity and reducing defect-mediated carrier losses. The $CsPb_{0.95}Ag_{0.05}I_3$ QDs, in particular, show the smallest bandgap variation ($\Delta E_g \approx 0.055$ eV) across 20–80 °C, demonstrating exceptional optical and thermal stability. These results underline that synergistic cation-halide engineering effectively mitigates phonon-driven bandgap fluctuations, offering a robust route for stabilizing perovskite QDs under elevated temperature operation.

3.5. FTIR analysis of surface functional groups and their temperature dependence in pristine and doped $CsPbI_3$ QDs

FTIR spectroscopy was employed to investigate the surface chemical environment and ligand-binding characteristics of pristine and doped $CsPbI_3$ QDs.[45] FTIR provides valuable insight into the vibrational modes associated with organic capping ligands and surface-bound species, which play a critical role in colloidal stability and defect passivation. The spectra of all three samples were collected in the range of 4000–500 cm^{-1} (see Fig. 6), enabling the identification of characteristic stretching and bending vibrations.

The FTIR spectra of pristine and doped $CsPbI_3$ QDs (Fig. 6a) exhibit similar characteristic vibrational features corresponding to the aliphatic C–H stretching (2957, 2924, 2857 cm^{-1}) and carboxylate (COO^-) stretching modes at 1461 cm^{-1} and 1378 cm^{-1}, as well as weaker C–O and C–H rocking bands at 1240 cm^{-1} and 724 cm^{-1}, respectively.[1,46] No additional peaks or significant wavenumber shifts are observed upon doping and halide passivation, indicating that the surface ligand chemistry remains unchanged. This consistency confirms that low-level Pb-site cation substitution and halide passivation simultaneously modify the lattice and defect structure without altering the organic capping environment of the QDs. FTIR peak positions and corresponding vibrational assignments for pristine and doped $CsPbI_3$ QDs are summarized in Table S5.

The temperature-dependent FTIR spectra (Fig. 6b–d) provide insight into the thermal evolution of surface ligands and their interaction with the perovskite lattice. In pristine $CsPbI_3$ QDs (Fig. 6b), the C–H and COO^- bands show a slight reduction in intensity above 60 °C, consistent with partial weakening of surface binding and the onset of ligand disorder, which aligns with the structural instability inferred from PL, XRD, and TEM results. Such changes are attributed to partial surface rearrangement and mild desorption of weakly bound OA/OAm molecules, which increase surface defect exposure at higher temperatures.

In contrast, both doped samples (Fig. 6c and d) exhibit remarkably stable FTIR profiles. Both $CsPb_{0.95}Co_{0.05}I_3$ and $CsPb_{0.95}Ag_{0.05}I_3$ QDs preserve all characteristic ligand-related FTIR peaks with nearly unchanged intensity across the examined temperature range, demonstrating excellent thermal stability of the surface coordination environment. This robustness originates from the synergistic effects of dual cation substitution and halide co-passivation, which strengthen surface bonding and suppress halide vacancies, effectively preventing ligand desorption and subsequent surface trap formation. As a result, the doped QDs maintain structural integrity and chemical passivation even under elevated temperatures.

The thermal stability observed in FTIR spectra strongly correlates with the optical responses of the QDs. In pristine

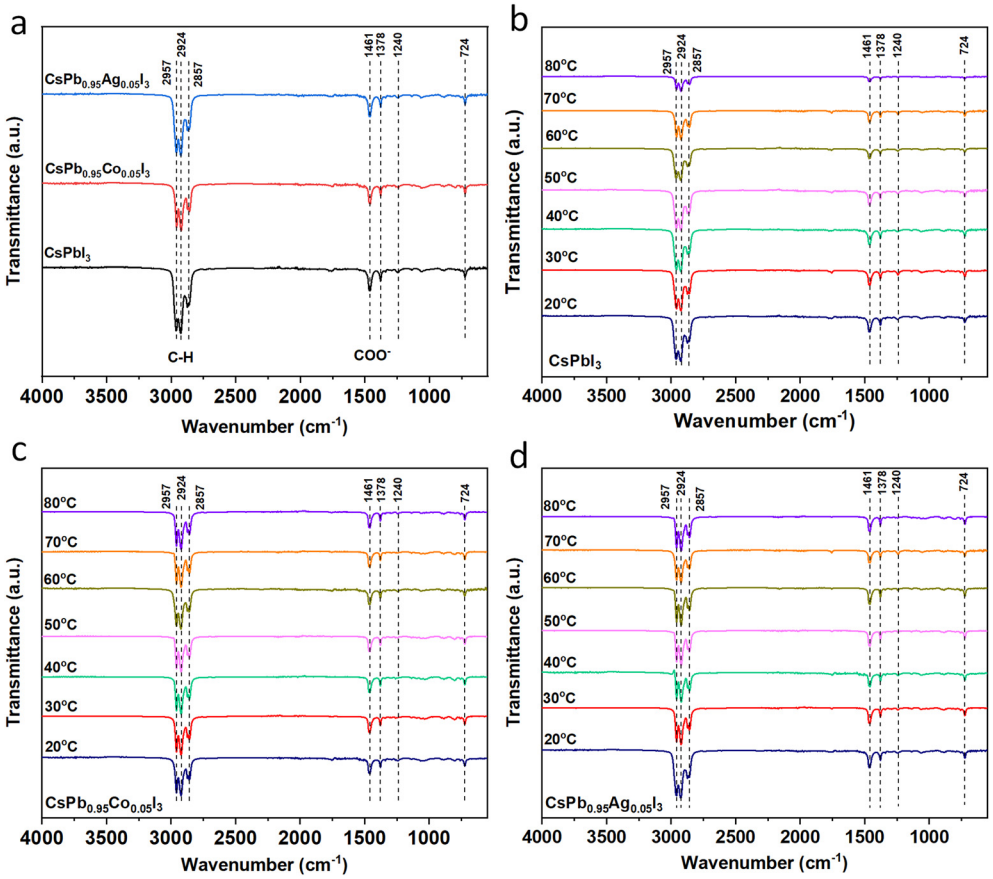

Fig. 6 (a) FTIR spectra of $CsPbI_3$, $CsPb_{0.95}Co_{0.05}I_3$ and $CsPb_{0.95}Ag_{0.05}I_3$ QDs, showing characteristic surface-ligand vibrations. The main absorption features correspond to aliphatic C–H stretching (2957, 2924, and 2857 cm^{-1}), asymmetric and symmetric carboxylate (COO^-) stretching (1461 and 1378 cm^{-1}), C–O stretching (1240 cm^{-1}), and C–H rocking (724 cm^{-1}). (b–d) Temperature-dependent FTIR spectra of pristine $CsPbI_3$, $CsPb_{0.95}Co_{0.05}I_3$ and $CsPb_{0.95}Ag_{0.05}I_3$ QDs recorded between 20 °C and 80 °C.

$CsPbI_3$ QDs, the slight attenuation of C–H and COO^- vibrations above 60 °C corresponds to the emergence of non-radiative decay channels observed in TRPL ($\Delta k_{nr} \approx 1.48 \times 10^{-2}$ ns^{-1}) and the pronounced PL quenching at elevated temperatures. The weakening of surface-ligand binding likely promotes the formation of shallow trap states and halide migration, accelerating carrier recombination and leading to reduced photoluminescence efficiency.

Conversely, the thermally stable FTIR spectra of the doped QDs correlate well with their suppressed nonradiative activation and superior PL retention. The doped samples, which exhibit only minor increases in Δk_{nr}, preserve ligand coordination up to 80 °C, confirming that cation incorporation alleviates lattice strain and reinforces surface anchoring. The synergistic effects of dual doping and halide passivation strengthen surface bonding and suppress halide vacancies, effectively preventing ligand desorption and the development of surface traps. As a result, the doped QDs maintain both structural integrity and chemical passivation even under thermal stress.

4. Conclusion

This study demonstrates that coupling Pb-site substitution with halide surface engineering provides an effective strategy to thermally stabilize all-inorganic $CsPbI_3$ QDs. Through systematic temperature-dependent analyses combining structural, optical, and spectroscopic characterization, we reveal that dual cation-halide doping ($CoCl_2$ + CoI_2 and AgCl + AgI) acts synergistically to enhance lattice rigidity and suppress thermally activated degradation. The doped QDs maintain their cubic α-phase integrity and intense photoluminescence up to 80 °C, while pristine $CsPbI_3$ undergoes structural distortion and PL quenching above 60 °C. TRPL measurements confirm that both Co- and Ag-substituted QDs exhibit markedly reduced nonradiative recombination rates ($\Delta k_{nr} \approx 6.7 \times 10^{-3}$ ns^{-1} and 5.6×10^{-3} ns^{-1}, respectively), reflecting efficient trap-state suppression. The smallest lattice dilation ($\Delta d \approx 0.6\%$) and minimal bandgap narrowing ($\Delta E_g \approx 0.055$ eV) observed in Ag-doped QDs underscore their superior thermal robustness.

Overall, this dual-modification approach establishes a clear structure–property relationship wherein Pb-site substitution strengthens the internal bonding network and halide passivation reinforces surface anchoring, jointly mitigating both bulk and interfacial instabilities. These insights provide a general design principle for engineering thermally resilient perovskite nanocrystals and lay the groundwork for reliable device implementation under elevated operating temperatures.

From an application perspective, the improved thermal robustness demonstrated here is directly relevant to perovskite QD optoelectronics, where localized heating during operation can accelerate degradation. In particular, greater resistance to thermally activated nonradiative losses and reduced lattice dilation are beneficial for QD-based emitters (LEDs and color-conversion layers) and photodetectors, in which junction temperatures can rise during sustained bias. Such thermal stabilization is expected to translate into improved emission stability, reduced efficiency roll-off, and enhanced operational lifetimes under continuous operation. More broadly, the temperature stabilization strategy established in this study with coupling Pb-site substitution and halide passivation provides a practical guideline for designing thermally resilient perovskite nanocrystals for operation under warm environments and thermal cycling.

Author contributions

Pouriya Naziri: data curation, formal analysis, investigation, methodology, writing original draft, writing – review & editing. Saba Sepahban Shahgoli: formal analysis, investigation, writing original draft, writing – review & editing. Hadi Jahangiri: formal analysis, investigation, writing original draft, writing – review & editing. Umut Aydemir: conceptualization, investigation, resources, supervision, funding acquisition, writing – review & editing.

Conflicts of interest

There are no conflicts to declare.

Data availability

The authors confirm that the data supporting the findings of this study are available within the article and its supplementary information (SI). Supplementary information: extended structural and optical analysis, recombination rate calculations, and FTIR vibrational characterizations for pristine and doped $CsPbI_3$ QDs, complementing the main manuscript. See DOI: https://doi.org/10.1039/d5nr04997k.

Acknowledgements

The authors would like to express their deep gratitude to Dr Gülcan Çorapçıoğlu from Koç University n^{2}STAR Center for her invaluable support with TEM characterization, and to Aslı Ceren Can for her assistance with FT-IR measurements.

References

1 Y. Li, M. Deng, X. Zhang, T. Xu, X. Wang, Z. Yao, Q. Wang, L. Qian and C. Xiang, *Nat. Commun.*, 2024, **15**, 5696.
2 Q. Shan, Y. Dong, H. Xiang, D. Yan, T. Hu, B. Yuan, H. Zhu, Y. Wang and H. Zeng, *Adv. Funct. Mater.*, 2024, **34**, 2401284.
3 P. Naziri, P. Simon, A. Onal, S. Nizamoglu, U. Aydemir and N. S. Peighambardoust, *ACS Appl. Nano Mater.*, 2024, **7**, 16735–16748.
4 N. S. Peighambardoust, E. Sadeghi and U. Aydemir, *ACS Appl. Nano Mater.*, 2022, **5**, 14092–14132.
5 J. A. Steele, V. Prakasam, H. Huang, E. Solano, D. Chernyshov, J. Hofkens and M. B. J. Roeffaers, *J. Am. Chem. Soc.*, 2021, **143**, 10500–10508.
6 J.-S. Yao, J. Ge, K.-H. Wang, G. Zhang, B.-S. Zhu, C. Chen, Q. Zhang, Y. Luo, S.-H. Yu and H.-B. Yao, *J. Am. Chem. Soc.*, 2019, **141**, 2069–2079.
7 B. Zhao, S.-F. Jin, S. Huang, N. Liu, J.-Y. Ma, D.-J. Xue, Q. Han, J. Ding, Q.-Q. Ge, Y. Feng and J.-S. Hu, *J. Am. Chem. Soc.*, 2018, **140**, 11716–11725.
8 P. Naziri, A. Onal, P. Simon, S. Sepahban Shahgoli, A. Yilmaz, N. S. Peighambardoust, S. Nizamoglu and U. Aydemir, *ACS Appl. Nano Mater.*, 2025, **8**, 20902–20914.
9 J. Ye, D. Gaur, C. Mi, Z. Chen, I. L. Fernández, H. Zhao, Y. Dong, L. Polavarapu and R. L. Z. Hoye, *Chem. Soc. Rev.*, 2024, **53**, 8095–8122.
10 Y. Chen, Y. Liu and M. Hong, *Nanoscale*, 2020, **12**, 12228–12248.
11 A. Swarnkar, A. R. Marshall, E. M. Sanehira, B. D. Chernomordik, D. T. Moore, J. A. Christians, T. Chakrabarti and J. M. Luther, *Science*, 2016, **354**, 92–95.
12 H. You, Z. Liu, K. Zhu, Q. Wang, Z. Liu, P. Li, X. Hu, J. Duan, Y. Li, N. Dai and X. Hou, *Nano Lett.*, 2025, **25**, 12446–12454.
13 D. Meggiolaro, E. Mosconi and F. De Angelis, *ACS Energy Lett.*, 2019, **4**, 779–785.
14 D. Kim, T. Yun, S. An and C.-L. Lee, *Nano Converg.*, 2024, **11**, 4.
15 S. Lim, S. Han, D. Kim, J. Min, J. Choi and T. Park, *Adv. Mater.*, 2023, **35**, 2203430.
16 S. Wang, Q. Zhao, A. Hazarika, S. Li, Y. Wu, Y. Zhai, X. Chen, J. M. Luther and G. Li, *Nat. Commun.*, 2023, **14**, 2216.
17 L. Bian, F. Cao and L. Li, *Small*, 2023, **19**, 2302700.
18 X. Ma, L. Yang, K. Lei, S. Zheng, C. Chen and H. Song, *Nano Energy*, 2020, **78**, 105354.
19 M. Liu, N. Jiang, Z. Wang, Y. Zheng, J. Hong, S. Du and D. Chen, *Adv. Photonics Res.*, 2021, **2**, 2100137.
20 C. Bi, X. Sun, X. Huang, S. Wang, J. Yuan, J. X. Wang, T. Pullerits and J. Tian, *Chem. Mater.*, 2020, **32**, 6105–6113.
21 Y. Xu, Q. Wang, L. Zhang, M. Lyu, H. Lu, T. Bai, F. Liu, M. Wang and J. Zhu, *Sol. RRL*, 2021, **5**, 2100669.

22 J. Shi, F. Li, J. Yuan, X. Ling, S. Zhou, Y. Qian and W. Ma, *J. Mater. Chem. A*, 2019, **7**, 20936–20944.
23 H. Jin, Y.-J. Zeng, J. A. Steele, M. B. J. Roeffaers, J. Hofkens and E. Debroye, *NPG Asia Mater.*, 2024, **16**, 24.
24 L. Hu, L. Duan, Y. Yao, W. Chen, Z. Zhou, C. Cazorla, C. H. Lin, X. Guan, X. Geng, F. Wang, T. Wan, S. Wu, S. Cheong, R. D. Tilley, S. Liu, J. Yuan, D. Chu, T. Wu and S. Huang, *Adv. Sci.*, 2022, **9**, 2102258.
25 X. Zhang, H. Huang, C. Zhao and J. Yuan, *Chem. Soc. Rev.*, 2025, **54**, 3017–3060.
26 J. Ye, M. M. Byranvand, C. O. Martínez, R. L. Z. Hoye, M. Saliba and L. Polavarapu, *Angew. Chem., Int. Ed.*, 2021, **60**, 21636–21660.
27 C. Deng, Q. Huang, Z. Fu and Y. Lu, 2024, *Nanomaterials*, 2024, **14**, 1201.
28 G. Pu, R. Wang, Y. Tang, J. Song and J. Wang, *Mater. Chem. Front.*, 2025, **9**, 1954–1970.
29 J. Shi, B. Cohen-Kleinstein, X. Zhang, C. Zhao, Y. Zhang, X. Ling, J. Guo, D. H. Ko, B. Xu, J. Yuan and W. Ma, *Nano-Micro Lett.*, 2023, **15**, 163.
30 M. Gramlich, C. Lampe, J. Drewniok and A. S. Urban, *J. Phys. Chem. Lett.*, 2021, **12**, 11371–11377.
31 O. Vukovic, G. Folpini, E. L. Wong, L. Leoncino, G. Terraneo, M. D. Albaqami, A. Petrozza and D. Cortecchia, *Nanoscale*, 2023, **15**, 5712–5719.
32 B. W. Boote, H. P. Andaraarachchi, B. A. Rosales, R. Blome-Fernández, F. Zhu, M. D. Reichert, K. Santra, J. Li, J. W. Petrich, J. Vela and E. A. Smith, *ChemPhysChem*, 2019, **20**, 2647–2656.
33 S. M. Lee, C. J. Moon, H. Lim, Y. Lee, M. Y. Choi and J. Bang, *J. Phys. Chem. C*, 2017, **121**, 26054–26062.
34 O. H. C. Cheng, T. Qiao, M. Sheldon and D. H. Son, *Nanoscale*, 2020, **12**, 13113–13118.
35 Q. Han, W. Wu, W. Liu, Q. Yang and Y. Yang, *J. Lumin.*, 2018, **198**, 350–356.
36 W. Zhou, F. Sui, G. Zhong, G. Cheng, M. Pan, C. Yang and S. Ruan, *J. Phys. Chem. Lett.*, 2018, **9**, 4915–4920.
37 B. Tang, L. J. Ruan, C. Qin, A. Shu, H. He and Y. Ma, *Adv. Opt. Mater.*, 2020, **8**, 2000498.
38 X. Yuan, S. Ji, M. C. De Siena, L. Fei, Z. Zhao, Y. Wang, H. Li, J. Zhao and D. R. Gamelin, *Chem. Mater.*, 2017, **29**, 8003–8011.
39 L. Zhang, C. Kang, G. Zhang, Z. Pan, Z. Huang, S. Xu, H. Rao, H. Liu, S. Wu, X. Wu, X. Li, Z. Zhu, X. Zhong and A. K.-Y. Jen, *Adv. Funct. Mater.*, 2021, **31**, 2005930.
40 Z. Chen, B. Zhou, J. Yuan, N. Tang, L. Lian, L. Qin, L. Zhu, J. Zhang, R. Chen and J. Zang, *J. Phys. Chem. Lett.*, 2021, **12**, 3038–3045.
41 X. Li, K. Wang, F. Lgbari, C. Dong, W. Yang, C. Ma, H. Ma, Z.-K. Wang and L.-S. Liao, *Nano Res.*, 2020, **13**, 2203–2208.
42 F. Li, Y. Liu, H. Wang, Q. Zhan, Q. Liu and Z. Xia, *Chem. Mater.*, 2018, **30**, 8546–8554.
43 I. Yeo, J. Dong Song and J. Lee, *Appl. Phys. Lett.*, 2011, **99**, 151909.
44 J. Ning, L. Zheng, W. Lei, S. Wang, J. Xi and J. Yang, *Phys. Chem. Chem. Phys.*, 2022, **24**, 16003–16010.
45 S. Xiang, W. Chen, F. Wan, L. Du, Z. Zhang, F. Zhou and Z. Jiang, *AIP Adv.*, 2021, **11**, 125120.
46 Q. Chen, F. Lei, Y. Shi, L. Yin, X. Ji, J. Xie, L. Zhang and L. Fan, *J. Lumin.*, 2023, **263**, 120108.